Eur. Phys. J. C 25, 67–75 (2002)
Digital Object Identifier (DOI) 10.1007/s10052-002-1015-x

THE EUROPEAN PHYSICAL JOURNAL C

Optical background measurement in a potential site for the NEMO KM^3 undersea neutrino telescope

F. Ameli[1,2], M. Bonori[1,2], F. Massa[1]

[1] Istituto Nazionale di Fisica Nucleare, Sezione di "Roma 1", 00133 Roma, Italy
[2] Università di Roma "La Sapienza", Dipartimento di Fisica, 00185 Roma, Italy

Received: 20 April 2002 /
Published online: 26 July 2002 –

Abstract. We describe the measurement of the deep sea optical background in some sites south of Capo Passero, Sicily. A continuous flux of about 440 photons cm^{-2} s^{-1} in the wavelength interval 440-550 nm is estimated due to the decays of the ^{40}K contained in the sea water. Bioluminescence light bursts are also observed and an example of time evolution is reported. All the measurements were accomplished using a deep sea module also described in this article.

1 Introduction

The construction of a cosmic neutrino telescope in the deep sea requires a detector with a very large sensitive volume, of the order of Km^3, in order to achieve a rate of a few events per year from faint galactic and extragalactic point sources [1]. High energy neutrino direction is reconstructed by analyzing muon tracks generated in primary interaction with seawater. High energy muons produce Čerenkov light and measuring photon arrival time on a telescope's optical sensors enables muon trajectory to be reconstructed. Thus the optical properties of seawater and the quantity of background light present are of fundamental importance in evaluating the performance of a neutrino telescope. As regards the optical properties of potential sites, the NEMO collaboration carried out a detailed study of light propagation properties at various locations, among which was the Ionian Sea off the south coast of Sicily, to which the measurements of background light reported in this paper refer [2]. As regards the quantity of optical activity present, light in the deep sea is produced not only by cosmic rays but also by decays of radioactive elements and by bioluminescent organisms. Sea salt contains potassium, whose isotope ^{40}K decays mostly β^- and by electron capture followed by a prompt γ, which in turn releases electrons by Compton scattering with the water molecules. Electrons with kinetic energy greater than 250 keV emit light in water by the Čerenkov effect. Because neutrino telescopes require a large light attenuation length, and this inevitably leads to a large sensitive volume of seawater, a considerable intensity of light coming from ^{40}K decays is to be expected, in spite of the small amount of this isotope present in sea salt. Such light is detected at a constant and relevant rate by PMTs deployed in the deep sea [3]. Furthermore, bioluminescent plankton emit light when stimulated and produce bursts of photons, typically lasting for several hundreds of milliseconds, at rates of up to several orders of magnitude greater than the ^{40}K signal. Moreover photobacteria emit light continuously [4] and their signals appear similar to those of ^{40}K, even if they may become modulated through time [5]. So far we have considered the optical activity present in the deep sea as the most relevant background for a neutrino telescope. Detailed knowledge of this background is of primary importance in designing the data acquisition electronics for the telescope. However the light coming from the ^{40}K decays, distinguished from bioluminescence, can be used as source for the optimization of the performance of optical modules (sensor and container) and even in the choice of the best sea site for the telescope itself. In fact the light spectrum present at a point of the sea, due to the ^{40}K decays in the surrounding volume, has the same characteristic shape of the light spectrum present at the same point and coming from neutrino interactions in the same volume. This happens because of two reasons: first, the light is produced in both cases with the typical $1/\lambda^2$ behavior of the Čerenkov spectrum; second, both neutrino interactions and ^{40}K decays are expected to be uniformly distributed in the sea volume. Thus Čerenkov light is filtered in the sea water by absorption and scattering, which are wavelength dependent, along the light trajectory from the point of production to the point of detection. This filtering is the same on average in both cases so that it produces equal average spectrum shapes. Thus, optimizing ^{40}K detection, neutrino detection is optimized as well. This is true both for the identification of the best suited optical module and for the choice of the optimal telescope site. In particular, the contribution of the ^{40}K decays to the single rate of a PMT can be used as a probe in the search for a telescope site, just looking for the site where

this contribution, normalized to the site salinity, is maximum. The calculation of the ^{40}K light spectrum at a depth of 2700 m in the KM3 site (see later) can be found in [3]. The Rome group of the NEMO Collaboration built an instrument, the "^{40}K module", to measure optical activity in the sea down to a depth of 3000 m. The performance of this ^{40}K module is summarized in Sect. 2. In this article we describe the data acquired during cruises in the year 2000 with the Research Vessel URANIA. The following cruises were undertaken:

- KM3 Site: south of Capo Passero (Siracusa, Sicily)
  Lat. 36°20' N, Long. 16°03' E
  site depth: 3310 m
  date: 21 March 2000
  reported as "KM3 March cruise"
- KM3 Site
  date: 28 September 2000
  reported as "KM3 September cruise"
- Test Site: off the port of Catania
  Lat. 37°33' N, Long. 15°23' E
  site depth: 1991 m
  date: 3 October 2000
- K40 Site: south of Capo Passero
  Lat. 36°36.6' N, Long. 15°36.6' E
  site depth: 3233 m
  date: 4 October 2000

In Sect. 3 we describe the data analysis and the statistical properties of the PMT rate. Measurement results at the above listed sites are reported in Sects. 4.1 and 4.2. In Sect. 4.3 bioluminescence events are described. In Sect. 5 we estimate the photon flux due to ^{40}K decays in KM3 on the basis of the measured rates.

2 The ^{40}K module

In this section we give a brief description of the main characteristics of the ^{40}K module described in greater details in [6]. The ^{40}K module is a stainless steel ISI316 cylinder (thickness 1.3 cm, height 51 cm, outer diameter 18 cm), within which a PMT (2" THORN EMI 9839A) and the read-out electronics are housed. A round window on one base of the cylinder is closed by 1.82 cm thick glass (Fig. 1). The PMT photocathode is in optical contact with the internal face of the glass through a 2 mm thick layer of silicon gel. The main components of the DAQ electronics [7] are an 8 bit Flash ADC, a high speed Field Programmable Gate Array (FPGA), a First In First Out (FIFO) memory and a Digital Signal Processor (DSP). The PMT signal is continuously sampled at 200 MHz by the 8 bit Flash ADC, which has a voltage input range from 0 V to -2 V (where 0 V corresponds to 255 ADC counts and -2 V to 0 counts). The FPGA receives the samples and implements a first level trigger, storing only "valid" events (those with at least one sample over threshold). The threshold can be dynamically set. When a signal is triggered, both the *threshold time* (i.e. the time when the pulse crosses the threshold level) and the event samples are stored in the FIFO until at least four consecutive

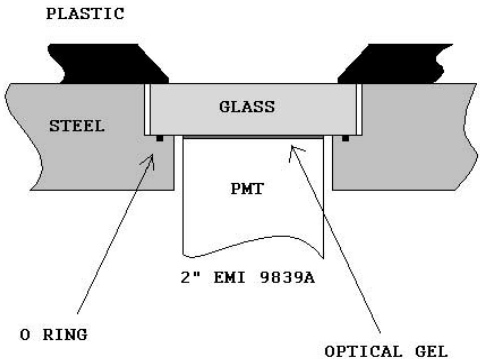

Fig. 1. Input window of the ^{40}K module. Dimensions are to scale with respect to the PMT 2" photocathode

values are under threshold, thus allowing the full pulse shape to be recorded. In each event some pre-trigger values sampled before the threshold time are also included. The threshold time is read on a 15 bit counter, the *Time Register*, clocked at 200 MHz. The Time Register wraps around every 135 μs and, at each wrap-around, is also reset by a hardware flag, allowing a timing coherence of 5 ns for periods longer than 135 μs. Every 1.5 μs the DSP checks the FIFO and, if it is not empty, reads and stores one word in a local memory until the requested number of words have been acquired. This set of data is referred to as a *Data Block*. After completion of each Data Block, acquisition is halted and the locally stored data are sent through the serial connection to the control PC on the research vessel. The FIFO is 20 kByte deep, which permits continuous sampling of a 100 μs signal with no dead time. During the cruises, the link between the ^{40}K module and the PC was realized by a pair of modems communicating at 9600 bps over the 4800 m long electro-mechanical cable of the URANIA oceanographic ship. This link, even though slow with respect to data rate, allowed the module to be continuously monitored. In each data acquisition run it was possible to determine the ADC pedestal, to set an optimal threshold value and to define the dimension and number of Data Blocks. In addition, a calibrated platinum resistor was used to measure the temperature inside the ^{40}K module. This value, which was transmitted at the beginning of each Data Block, reached its constancy in few minutes, showing that there was good heat exchange between the ^{40}K module and the surrounding water. The PMT working point at the level of the single photoelectron (s.p.e.) was set pulsing a green LED and attenuating the light with absorbers in order to obtain a light beam mostly consisting of single photons. Figure 2 shows the charge of these events (dots) and a fit function (continuous line) composed by a gaussian curve, describing the s.p.e. events, and a decreasing exponential curve, describing the events at low PMT gain. At the 2400 V working point the PMT gain is $7.5{\cdot}10^7$. In order to extract from the rate measured in the deep sea the physical characteristics of the site, we define the sensitivity $\Gamma(\lambda)$ of the ^{40}K module at the s.p.e. as the PMT rate produced by a unitary flux at a given wavelength λ. Assuming that the detected events in the deep sea are due to s.p.e., the PMT rate R,

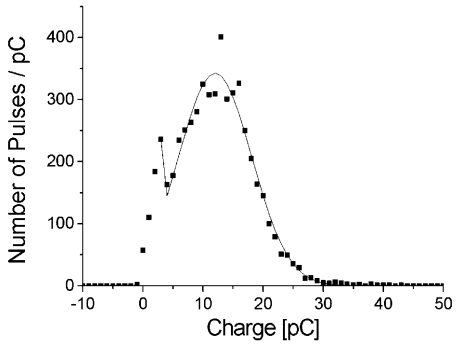

Fig. 2. Charge of events generated by a single photon beam (*dots*) and a fit function (*continuous line*)

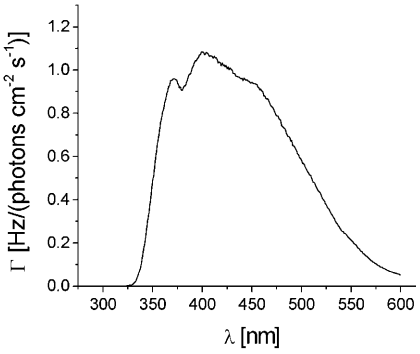

Fig. 3. Sensitivity of the ^{40}K module defined as the PMT rate produced by a unitary photons flux at a given λ

after subtracting the dark current and compensating for the threshold rate loss, can be written as

$$R = \int_{\lambda_1}^{\lambda_2} \Phi(\lambda)\ \Gamma(\lambda)\ d\lambda$$

where $\Phi(\lambda)$ [photons $cm^{-2}s^{-1}nm^{-1}$] is the photon flux at wavelength λ and $\Gamma(\lambda)$ is

$$\Gamma(\lambda) = S\ QE(\lambda)\ \eta(\lambda) \qquad (1)$$

where S is the photocathode area, $QE(\lambda)$ the photocathode quantum efficiency and $\eta(\lambda)$ the acceptance of the ^{40}K module input window. Figure 3 shows the sensitivity of the ^{40}K module, resulting from a photocathode CB value of 7.3, as quoted by the manufacturer, and from the measured optical properties of module input window.

3 Data analysis

3.1 Rate measurement

In Fig. 4 we show a typical single photoelectron PMT pulse detected in the deep sea and sampled by the fast ADC. The threshold was set at count 244 (i.e., signals with at least one sample less than or equal to 244 were accepted) to cut electronics noise, the average value of which was 250.4. The s.p.e. pulse reported in Fig. 4 consists of ten

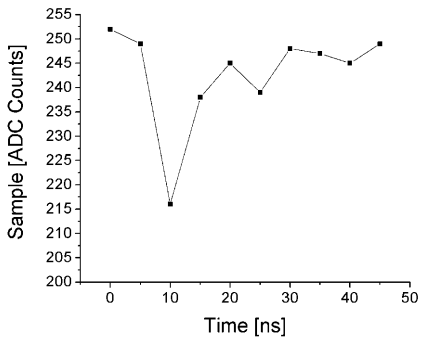

Fig. 4. Typical s.p.e. PMT pulse sampled by the fast ADC

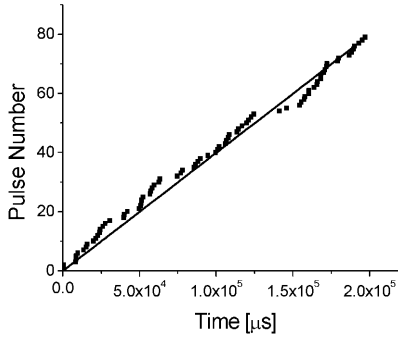

Fig. 5. Pulse number as a function of time and *linear fit* for a *data block* (slope R = 373 Hz)

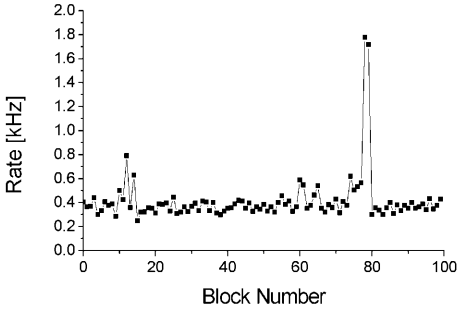

Fig. 6. Sequence of rates measured at a depth of 2700 m in KM3

ADC samples, two under and eight over threshold. The first sample gives the offset value for the subsequent ones: this method of pedestal subtraction optimizes the charge resolution. The Time Register value corresponding to the third sample is the event threshold time. Figure 5 shows an example of the analysis of a data block acquired during the run performed during the March cruise in KM3. This block contains 83 PMT pulses recorded in about 200 ms. In the Figure the pulse number and its linear fit are plotted as a function of arrival time. The slope of the linear fit gives the block event rate, R (373 Hz for the events represented in Fig. 5). The particular distribution around the straight line is due to Poisson statistics, which favors small, rather than large, delays between consecutive pulses, as will be explained later. The sequence of block rates of a typical run performed during the KM3 September cruise is shown in Fig. 6. Each individual value of the sequence is the linear

fit slope of a corresponding data block representation, like that shown in Fig. 5. Two regimes of photon production appear in Fig. 6: the first is related to the clear plateau of rates, the second to bursts of photons, which last for a short time, at a higher rate. Taking into account that the contribution of PMT dark current (32 Hz on average) is negligible, the first regime can be attributed mainly to light coming from ^{40}K decays ("^{40}K events") and the second to bioluminescence.

3.2 Rate statistics

In order to go deeper into the data analysis, we will calculate the statistical behavior of the plateau signal rate. Let us suppose that events are produced by a stochastic process at a constant rate. This means that the expectation value $\langle R \rangle$ of the rate of events does not depend on time and that all variations observed among data blocks are due only to statistical fluctuations. In our data acquisition the number of pulses acquired per data block does not depend on the physical rate, but only on the duration of pulses and on the predefined dimension of the data block. We measure the rate R of the events in a data block from the slope of the linear fit to the plot of pulse number against pulse time, as in Fig. 5. Let us start working with a constant number of pulses per data block, $n+1$, numbered from 0 to n. The time elapsed between the first and the last pulse can be obtained from the fit by:

$$t = \frac{n}{R} \tag{2}$$

It is clear that

$$t = \tau_1 + \tau_2 + \ldots + \tau_n \tag{3}$$

where τ_k is the delay of the k^{th} pulse compared to that of the $(k-1)^{th}$. The probability $g(\tau)\ d\tau$ of having a delay between any two consecutive pulses from τ to $\tau + d\tau$ is equal to the probability of having zero pulses in time τ and one in $d\tau$. If μ is the expectation value of the delay τ, from Poisson statistics we have

$$g(\tau)d\tau = \frac{d\tau}{\mu}\ e^{-\frac{\tau}{\mu}} \tag{4}$$

The variance of τ can be calculated from (4):

$$v(\tau) = \mu^2$$

The probability density function $F_n(t)$ of time t can be deduced from $g(t)$. In fact, for $n = 1$, we have $F_1(t) = g(t)$. For $n = 2$ we have

$$t = \tau_1 + \tau_2$$

If we consider all the possible pairs τ_1 and τ_2 which can be added to give t, we have

$$F_2(t) = \int_0^t g(\tau)g(t-\tau)d\tau = \frac{e^{-\frac{t}{\mu}}}{\mu}\frac{t}{\mu}$$

We can write in general

$$F_n(t) = \int_0^t g(\tau)F_{n-1}(t-\tau)d\tau \tag{5}$$

Because $F_2(t)$ is known, (5) allows $F_3(t)$ to be calculated, and so on. So we have

$$F_n(t) = \frac{e^{-\frac{t}{\mu}}}{\mu}\left(\frac{t}{\mu}\right)^{n-1}\frac{1}{(n-1)!} \tag{6}$$

This result is clear because $F_n(t)dt$ is equal to the probability dt/μ of having one pulse in dt multiplied by the probability of having n pulses in t. This, in turn, is equal to the probability of having time t composed of $n-1$ delay intervals τ, which, for Poisson statistics, is:

$$e^{-\frac{t}{\mu}}\left(\frac{t}{\mu}\right)^{n-1}\frac{1}{(n-1)!}$$

The expectation value $\bar{t}$ and the variance $v(t)$ of time t, for constant n, can be calculated from (6):

$$\bar{t} = \int_0^\infty F_n(t)tdt = n\mu \tag{7}$$

$$v(t) = \int_0^\infty F_n(t)(t-\bar{t})^2dt = n\mu^2 \tag{8}$$

The inverse of the measured value of the rate R of a data block gives a sample of the expectation value μ. In fact, the mean value of the delay τ in the data block is, from (2),

$$\overline{\tau} = \frac{\tau_1 + \tau_2 + \ldots + \tau_n}{n} = \frac{t}{n} = \frac{1}{R} \tag{9}$$

The probability density function of the mean delay $\overline{\tau}$ can be derived from (6):

$$f_n(\overline{\tau}) = F_n(n\overline{\tau})\frac{dt}{d\overline{\tau}} = \frac{n}{\mu}\left(\frac{n\overline{\tau}}{\mu}\right)^{n-1}\frac{1}{(n-1)!}\ e^{-\frac{n\overline{\tau}}{\mu}} \tag{10}$$

This function coincides with $g(\tau)$ (see (4)) in the case of two pulses per data block ($n = 1$). The expectation value of $\overline{\tau}$ is

$$\int_0^\infty f_n(\overline{\tau})\overline{\tau}d\overline{\tau} = \int_0^\infty F_n(t)\frac{t}{n}dt = \mu$$

and the variance

$$v(\overline{\tau}) = \int_0^\infty F_n(t)\left(\frac{t}{n} - \mu\right)^2 dt = \frac{\mu^2}{n}$$

In real cases, due to the variability in the duration of events, the number of pulses in a data block, for a fixed block dimension, is not constant. The distribution function $P(n)$ of the number of pulses per data block is obtained experimentally. Thus the probability density functions of time t and of the mean delay $\overline{\tau}$ become, respectively

$$H(t) = \sum_n P(n)F_n(t)$$

and

$$G(\overline{\tau}) = \sum_n P(n) f_n(\overline{\tau}) \tag{11}$$

Because n is independent of t, we have

$$\bar{t} = \int_0^\infty H(t) t dt = \sum_n P(n) \int_0^\infty F_n(t) t dt$$

and using (7)

$$\bar{t} = \sum_n P(n) n\mu = \overline{n}\mu$$

To calculate the variance

$$v(t) = \int_0^\infty H(t) \left(t - \overline{n}\mu\right)^2 dt$$

we can put

$$t - \overline{n}\mu = (t - n\mu) + (n - \overline{n})\mu$$

and we have

$$\begin{aligned} v(t) = & \sum_n P(n) \int_0^\infty F_n(t) \left(t - n\mu\right)^2 dt \\ & + \sum_n P(n) \int_0^\infty F_n(t) \left(n - \overline{n}\right)^2 \mu^2 dt \end{aligned}$$

Using (8) we have

$$\begin{aligned} v(t) &= \sum_n P(n) n\mu^2 + \sum_n P(n) \left(n - \overline{n}\right)^2 \mu^2 = \\ &= \mu^2 \left(\overline{n} + v(n)\right) \end{aligned}$$

In the same way we can calculate the expected value and the variance of $\overline{\tau}$, which are, respectively, equal to μ and μ^2/n. So that

$$\frac{v(t)}{\bar{t}^2} = \frac{1}{\overline{n}} + \frac{v(n)}{\overline{n}^2}$$

and

$$\frac{v(\overline{\tau})}{\mu^2} = \frac{1}{\overline{n}}$$

The same values of $v(t)$ and $v(\overline{\tau})$ can be obtained directly from (3) and (9):

$$v(t) = \mu^2 v(n) + \overline{n} v(\tau) = \mu^2 (\overline{n} + v(n))$$

$$v(\overline{\tau}) = \frac{v(\tau)}{\overline{n}} = \frac{\mu^2}{\overline{n}}$$

From (9) we also have

$$\frac{v(R)}{R^2} = \frac{v(\overline{\tau})}{\mu^2} = \frac{1}{\overline{n}} \tag{12}$$

From what we have said so far it is clear that we can proceed to analyze the data by grouping data block events in an arbitrary number m of consecutive pulses, ranging from a minimum of two up to the total number in the data block $(n + 1)$. For a fixed number m $(< n + 1)$, the distribution density function of the average delay of the events in the group is represented by (10) with $n = m$. On the other hand, (11) represents the distribution for the case where groups are composed of the total number of data block pulses. In the following section we report the statistical analysis of the two extreme cases, those in which $m = 2$ and $m = n + 1$. From (12) it is clear that the relative resolution of the rates of a plateau such as that in Fig. 5 is expected to be $1/\sqrt{n}$, if these events are produced in a stochastic process with a rate expectation value independent of time.

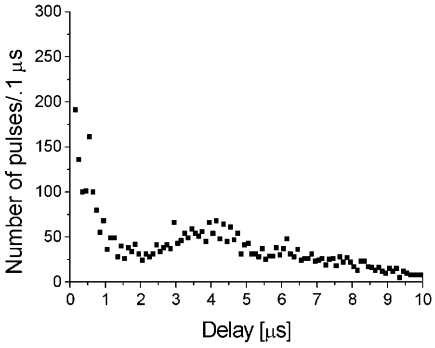

Fig. 7. Distribution of delays between consecutive pulses at small delay values

4 Results

4.1 Results in KM3 and K40

In the KM3 September cruise we measured the PMT rate, at a depth of 2700 m, during ten consecutive runs distributed over about eight and half hours. In each run, consisting of 100 data blocks, the rate was sampled for about seven minutes. Because of the transmission dead time, the average effective active time per run was 20.7 s. We start analyzing the events of the KM3 September cruise using the delay distribution between two consecutive pulses. First, the data were corrected for the events contributing to small delay values, up to a few tens of microseconds (Fig. 7). These events, which are mainly attributable to bioluminescence and PMT refirings, are excluded from the analysis of ^{40}K events. Figure 8 shows the delay distribution compared with the exponential function $g(\tau)$ (see (4)), fitting delay values greater than 40 μs. The coefficient of this exponential function gives the average rate

$$\overline{R}_{un} = 371.5\ Hz \tag{13}$$

Using this fit function, we were able to find the number of good events excluded in the calculation of (13) because of the delay value less than 40 μs. This number is 2.1% of the total events and the corrected rate is

$$\overline{R}_{cor} = 376.9\ Hz \tag{14}$$

We applied a further correction because of the rate loss due to the electronics threshold. We proceeded filtering

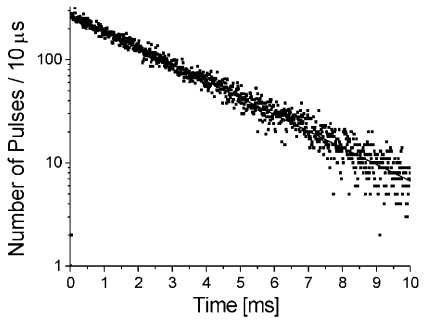

Fig. 8. Distribution of delays between consecutive pulses and exponential fit (KM3 September cruise run). The exponential fit coefficient gives the average rate for the run (371.5 Hz)

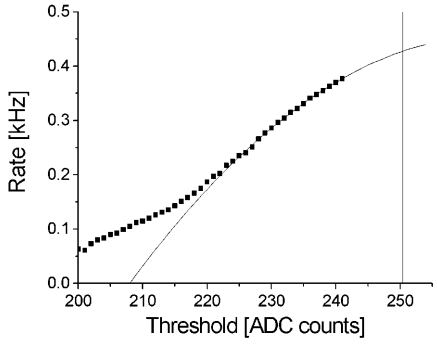

Fig. 9. Data filtered at various thresholds showing a rate of 427.6 Hz at the offset value of 250.4 ADC counts

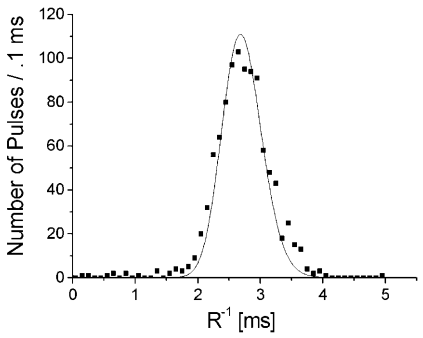

Fig. 10. Distribution of the inverse of the rate during the KM3 September cruise and data fit ($\overline{R}_G = \frac{1}{\mu} = 367.8\ Hz$)

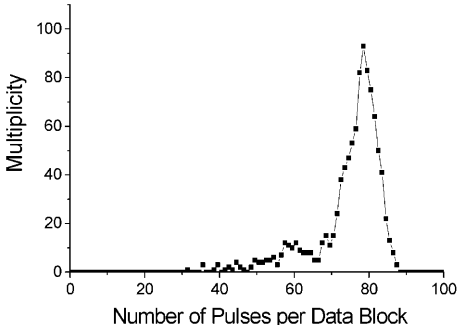

Fig. 11. Histogram of the number of pulses per data block during the KM3 September cruise (average value 74.7)

the data at different threshold levels, calculating the new rates, fitting these rates with a polynomial and extrapolating down to the electronics offset [6]. This result is shown in Fig. 9 where a rate of 427.6 Hz is obtained at the offset value of 250.4 ADC counts. Subtracting the 37.1 Hz of the dark current rate, calculated using the same extrapolation procedure, we obtain

$$\overline{R} = (390.5 \pm 1.5)\ Hz \tag{15}$$

We attribute the rate (15) to ^{40}K events, with a further uncertainty of 15 Hz due to systematic errors.

In Fig. 10 we will now analyze the same events of KM3 September cruise using the distribution of the inverse of the rate R of the data blocks. Events with delay smaller than 40 μs were excluded from this analysis, as in Fig. 8. In Fig. 10 we compare the experimental values with those expected from a stochastic mechanism of photon production, the distribution density function of which is (11). Figure 11 shows the distribution of the number of pulses per data block obtained for these runs, with an average value of 74.7 pulses per data block. The normalized distribution gives the function $P(n)$ used in (11). The best fit of $G(\overline{\tau})$ to the experimental data produces the average rate of the events in the plateau

$$\overline{R}_G = \frac{1}{\mu} = (367.8 \pm 1.6)\ Hz \tag{16}$$

This value has to be compared with the uncorrected rate (13). We want to stress that the width of the fit function in Fig. 10 is not an independent parameter, rather it is intrinsic to the $G(\overline{\tau})$ function and depends exclusively on the average number of data block pulses (see (12)):

$$\frac{\sigma(R)}{R} = \frac{\sigma(\overline{\tau})}{\overline{\tau}} = \frac{1}{\sqrt{n}} \tag{17}$$

Data in Fig. 10 give $\sigma(R)/R = 14.8\%$, while data in Fig. 11 yield a $1/\sqrt{n}$ value of 11.6%. Condition (17) helps in distinguishing the ^{40}K signals from the bioluminescence background, because any possible "bump" in the $\overline{\tau}$ distribution needs the width expected from the $G(\overline{\tau})$. We conclude this analysis stating that the observed time distribution of the ^{40}K events follows the Poisson statistics. Figure 12 shows the average rate of each run of the September cruise as a function of the run start time.

In the March cruise in KM3 we measured the PMT rates at a depth of 2800 m in four successive runs, distributed over about one and half hours, for a total active time of 164 s. During this first cruise the ^{40}K module was partially shadowed by the containers of other instrumentation (this shadowing was removed for the subsequent cruises). Figures 13 and 14 show events acquired in the March cruise in KM3 which are analogous to events represented in Figs. 10 and 12. Figure 13 displays at least two peaks; however function (11) fits only the rightmost peak. The events of the unfitted peak do not follow the ^{40}K events statistics. The better resolution of event distribution in Fig. 13 compared to Fig. 10 is due to a greater number of pulses per data block.

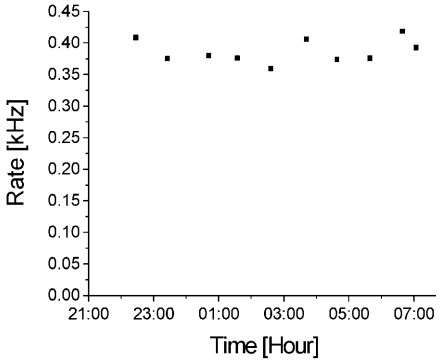

Fig. 12. Average plateau rates of each run performed during the KM3 September cruise as a function of run start time

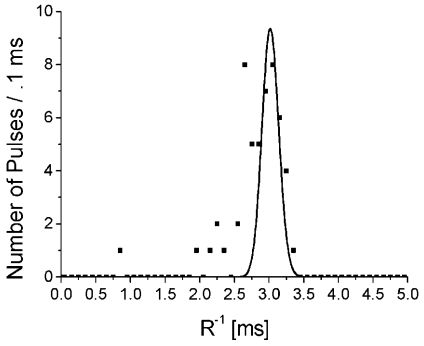

Fig. 13. Same as Fig. 10 but with higher number of events per data block (KM3 March cruise)

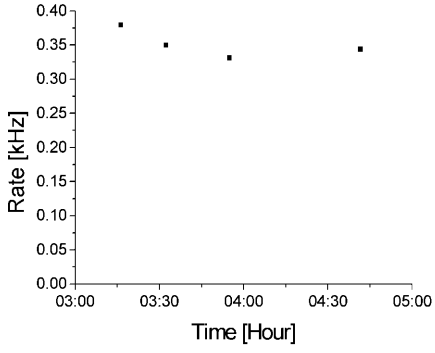

Fig. 14. Same as Fig. 12 for the four runs of the KM3 March cruise

Data taken in K40 at varying depths are shown in Fig. 15.

Taking into account the effect of the shadowing during the KM3 March cruise (which was calculated by Montecarlo as a loss of acceptance of 14%), the above results show the contribution to the PMT rate attributable to ^{40}K decays as constant over a total run time of ten hours, distributed through different seasons of the year. Figure 16 shows the charge of ^{40}K events. Compared to the charge distribution obtained calibrating the PMT by a LED source (Fig. 2 of [6]), it is clear that the peak-to-valley separation is not visible any longer. This different behavior in the experimental condition is due to an offset level noise greater than the one found during the calibration. Figure 17 shows the histograms of the offset level measured in the two conditions. Taking into account this noise effect, we conclude that the presence of ^{40}K events with charge greater of the s.p.e. is negligible.

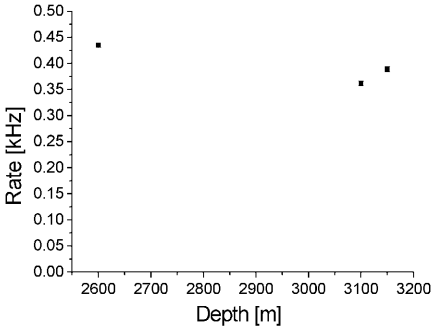

Fig. 15. Rates of plateau measured in the K40 site at varying depths

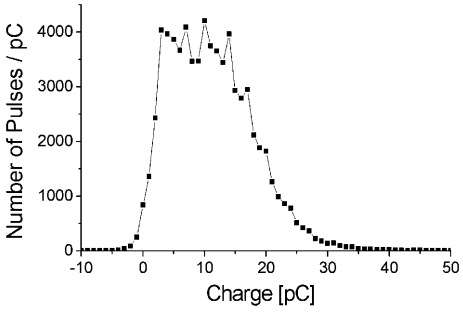

Fig. 16. Charge distribution of ^{40}K events

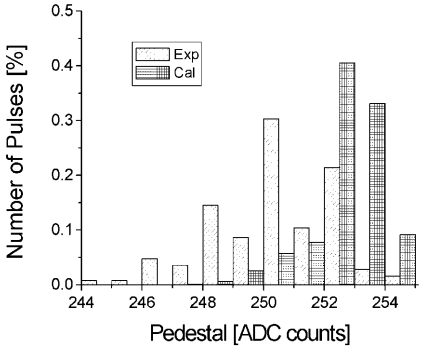

Fig. 17. Histogram of pulse pedestals in experimental and calibration conditions

4.2 Results in the test site

In the Test Site we measured PMT rates at various depths down to 1950 m (Fig. 18). The signal stability was measured for about four hours at a depth of 1500 m (Fig. 19); the average rate was 1100 Hz. In Fig. 20 the sequence of the rates at a depth of 1000 m is shown by way of example. Compared to KM3 (see Fig. 6) there are two clear differences: a significant presence of bioluminescent signals and a higher plateau value. The difference in salinity between the two sites [2] (i.e. in the quantity of ^{40}K in the seawater) is negligible, and therefore this can not account for

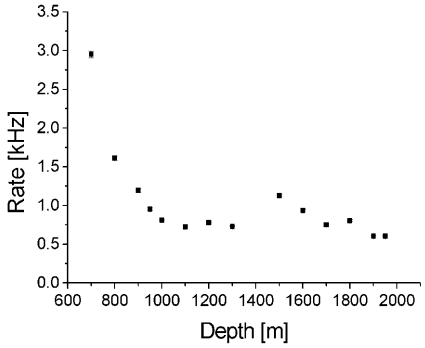

Fig. 18. Rates of plateau at various depths in the Test Site

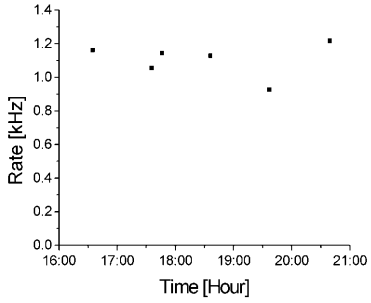

Fig. 19. Rates of plateau as a function of run start time at a depth of 1500 m in the Test Site

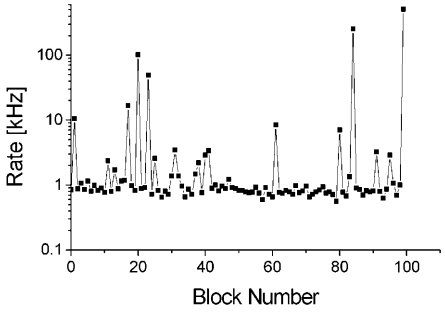

Fig. 20. Sequence of rates at a depth of 1000 m in the Test Site

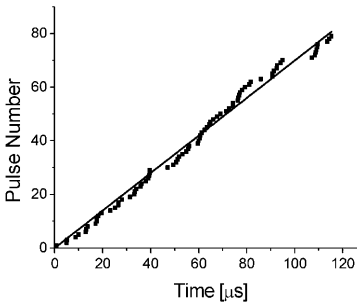

Fig. 21. Pulse number as a function of time (*dots*) and linear fit (*continuous line*) for a data block (slope R = 725 kHz)

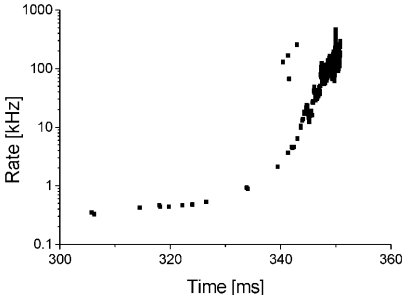

Fig. 22. Primer of a bioluminescence event rate as a function of time

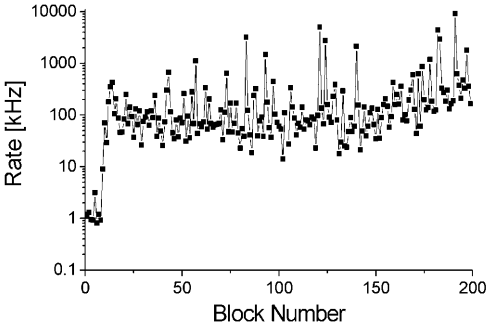

Fig. 23. Sequence of rates measured during ^{40}K module recovery in Test Site. The initial step marks the start of the recovering

the difference between the two plateau values obtained. Further investigation is needed to establish whether the higher plateau value for the Test Site is due to the presence there of additional radioactive elements contained in dusts from the Etna volcano, or whether it is due to an effect of bioluminescence, as was observed in the Antares site [5].

4.3 Bioluminescence events

Bioluminescence events appear either as a single bunch of pulses of significantly high rate, as in Fig. 21 where 725 kHz are measured, or as an accumulation of events at small time values in the delay distribution (Fig. 8). This high rate usually fills the available electronics memory quickly, so the number of events recorded in a data block is just a small fraction of the entire bioluminescence event which is occurring. This is evident in Fig. 21, which shows about 80 consecutive pulses at constant average rate recorded during an interval of about 115 μs. In Fig. 22 the primer of a bioluminescence light pulse is shown. The Figure shows an increase in the rate within the space of a few milliseconds, from a value of 370 Hz (attributable to ^{40}K events) to a value at least three orders of magnitude greater, before the acquisition stops. The time dependence of the bioluminescence rate is well described by a function proportional to

$$e^{\frac{t}{T}} \tag{18}$$

with T = 2 ms, indicating a possible avalanche mechanism of light production. In order to increase the statistical significance of bioluminescence events in Test Site, data were acquired during the recovery of the ^{40}K module, when the movement of the apparatus stimulated the production of bioluminescence light (Fig. 23). The charge distribution of events in Fig. 23 is shown in Fig. 24. Comparing Fig. 24

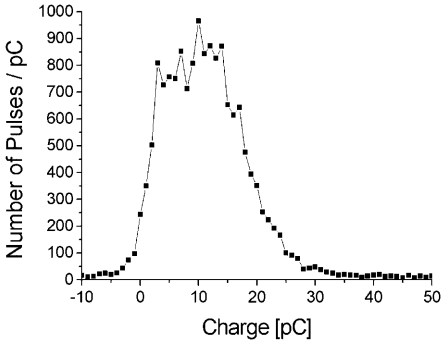

Fig. 24. Charge distribution of events in Fig. 23

and Fig. 16, it is clear that bioluminescence events consist mainly of s.p.e. signals. The same charge distribution was measured in all the three sites. Thus we observed bursts of bioluminescence light composed by single photons emitted at modulated frequency.

5 Conclusions

A time constant photon flux, attributed to ^{40}K decays, was observed in KM3, south of Capo Passero, at a depth of 2800 m. The measurements were confirmed after a period of six months. PMT charge distribution of observed ^{40}K signals is mainly composed of single photoelectrons. Considering $\Gamma(\lambda)$, as defined in (1), constant and equal to its average value $\overline{\Gamma}$ in the range $350 < \lambda < 500\ nm$, we have for the KM3 site

$$\int_{350\ nm}^{500\ nm} \Phi(\lambda)\ d\lambda \simeq \frac{R}{\overline{\Gamma}} \simeq 440\ photons\ cm^{-2}s^{-1} \quad (19)$$

where R = 390.5 Hz and $\overline{\Gamma} = 0.89\ \frac{Hz}{photons\ cm^{-2}s^{-1}}$. Results from the K40 site are compatible with the KM3 measurements. Higher PMT rates, depending on depth, were observed in the Test Site off the port of Catania. Further investigation is needed to explain these higher rates. Bioluminescence light was also detected as composed of single photons, independently of site. Bioluminescence primers showing an avalanche-like mechanism of light production were observed.

Acknowledgements. We are indebted to R. Masullo, L. Pappalardo and M. Petruccetti for the help given during the cruises. We thank captains Lubrano and Gentili and all the crew of the research vessel URANIA for technical help and support during deployment operations.

References

1. T. K. Gaisser, F. Halzen, T. Stanev. Particle astrophysics with high energy neutrinos. Phys. Rept. **258**, 173–236 (1995)
2. NEMO Collaboration Capone et al. Site Characterization for a Km^3 Scale Deep Underwater Neutrino Observatory in the Mediterranean Sea, volume 2. HE.6.3.04, Salt Lake City, 1999
3. F. Massa. Optical radiation background from ^{40}k decays in undersea neutrino telescopes. Eur. Phys. J. C, **22**(4), 749–756 (2002)
4. C. D. Mobley. Light and Water. Academic Press, New York, 1994
5. P. Amram et al. Background light in potential sites for ANTARES undersea neutrino telescope. Astroparticle Physics **13**, 127–136 (2000)
6. F. Ameli et al. A single photon detector for the measurement of optical radiation in the deep sea. Submitted to Review of Scientific Instruments
7. F. Ameli et al. Data acquisition electronics for NESTOR deep sea neutrino telescope: Project and tests. NIMPR A **423**, 146–156 (1999)